Versatile Molecular Engineering of *In Situ* Cross-Linked Multifunctional Electrolytes for Long-Lifetime and Safe Semisolid Lithium Metal Batteries

Kai Chen, Anjun Hu,* Guo-Rui Zhu, Yuanjian Li, Jingyun Jiang, Borui Yang, Ting Li, Kun Li, Jingze Chen, Wang Xu, Zhen Wang, Ruize Xu, Wei Yang, Jian Wang, Gang Wu,* Jianping Long,* and Zhi Wei Seh

ABSTRACT: The practical application of semisolid lithium metal batteries is impeded by inadequate ionic conductivity, suboptimal oxidation/reduction stability, and safety concerns of the electrolyte. Herein, a versatile molecular engineering strategy is proposed to construct a robust polymer framework for semisolid electrolytes, which creates highly compatible cross-linked networks by the in situ gelation of concentrated succinonitrile-based plastic crystal electrolytes and multifunctional nitrogen- and fluorine-rich monomers. This strategy allows the electrolyte to promote rapid Li-ion transpsort through weak coordination with the polymer segments. Meanwhile, the strong interactions between the polymer matrix and succinonitrile enhance their mutual solubility, reduce the crystallinity of succinonitrile, and establish fast ion-conductive pathways. The resultant electrolyte induces the formation of LiF/Li_3N-rich solid electrolyte interphases and achieves uniform lithium deposition behaviors. Moreover, it mitigates fire risks by cothermally decomposing to produce fire-extinguishing gases (CO_2 and NH_3) and leveraging the nonflammability of succinonitrile. Significant improvements in electrochemical performance have been observed in Li symmetric, Li||$LiFePO_4$, and Li||$LiNi_{0.8}Co_{0.1}Mn_{0.1}O_2$ cells both at room temperature and high temperature (60 °C). As a demonstration model, this molecular engineering strategy has been successfully applied to enhance thermal stability and safety in Li||$LiNi_{0.8}Co_{0.1}Mn_{0.1}O_2$ pouch cells, offering a promising solution for semisolid lithium metal batteries under extreme conditions.

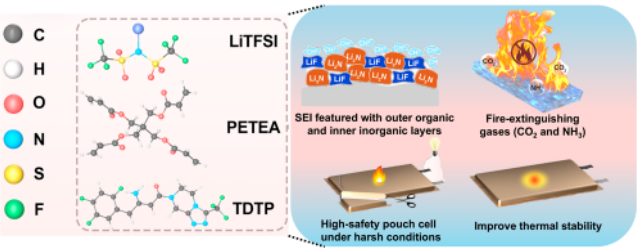

KEYWORDS: *semisolid batteries, lithium metal batteries, molecular engineering, multifunctional electrolytes, in situ cross-linking*

Conventional graphite intercalated lithium-ion batteries are increasingly inadequate for meeting the escalating energy demands of emerging applications.[1] Lithium metal anodes, with its extremely high specific capacity (3860 mAh g^{-1}) and very low redox potential (−3.04 V vs Li/Li^+), have emerged as a promising candidate for next-generation energy storage systems.[2,3] However, the practical deployment of lithium metal batteries (LMB) remains hampered by significant challenges, largely attributable to the limitations of current electrolyte technologies.[4,5] Commercially available carbonate and ether electrolytes are unsuitable for LMBs.[6] Specifically, unstable solid electrolyte interphases (SEI) in carbonate electrolytes can lead to lithium dendrite growth, shortening the cycle life of the battery and even triggering short circuits.[7,8] Ether electrolytes, on the other hand, have poor oxidative stability at high voltages (>4 V vs Li/Li^+) and are prone to uncontrolled solvent decomposition on the cathode surface, accelerating battery performance degradation. In addition, both are volatile and flammable, which can easily cause safety problems.[9−14]

Solid-state electrolytes represent a promising alternative to conventional liquid electrolytes. However, solid polymer electrolytes are limited by poor oxidative or reductive stability

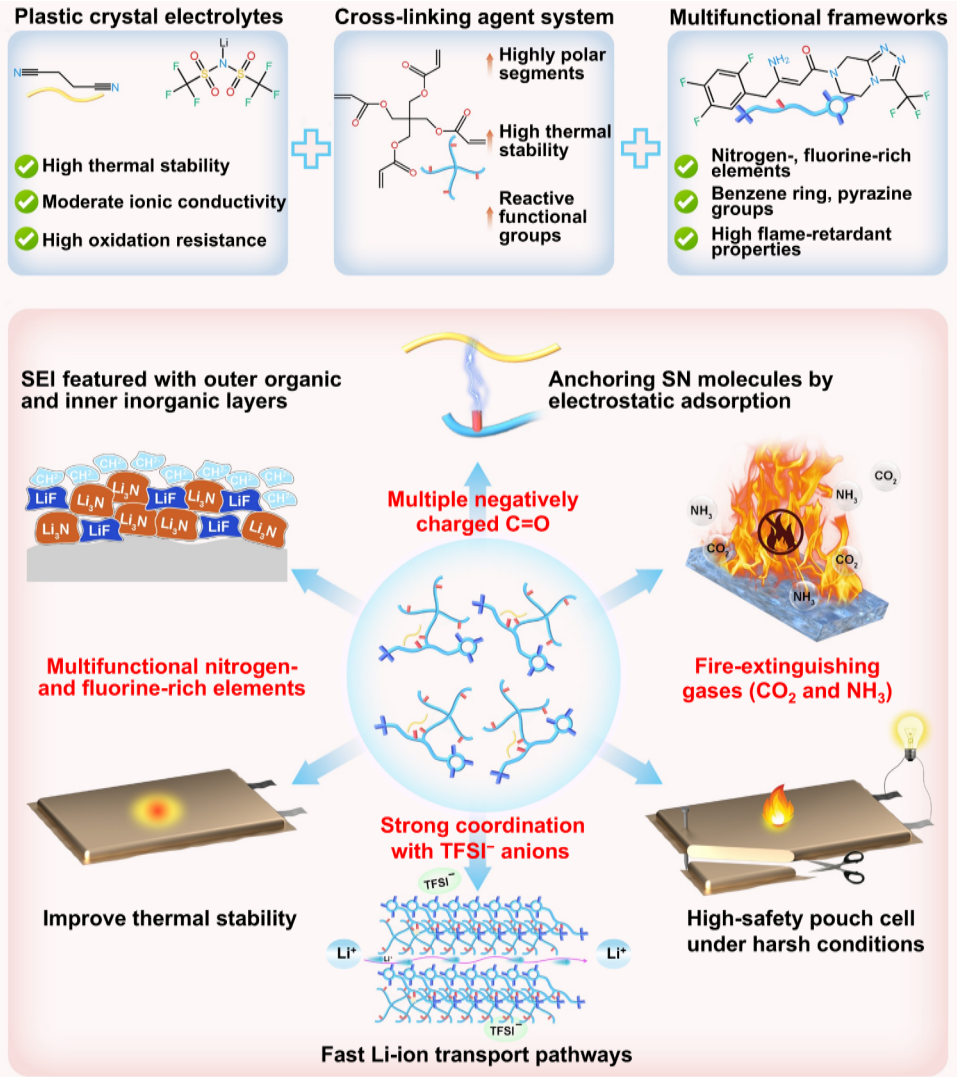

Figure 1. Illustration of the versatile multifunctional molecular design concept for G-TSL-based semisolid polymers.

and slow ion transport kinetics.[1] Inorganic ceramic electrolytes have high ionic conductivity but are brittle, complex and have poor interfacial contact. In contrast, solid plastic crystal electrolytes (SPCE) based on succinonitrile (SN) stand out due to their high oxidation resistance, high thermal stability, nonflammability, and moderate ionic conductivity.[15] The highly polar cyano group (−C≡N) at both ends of the SN molecule effectively solubilizes lithium salts and facilitates the rapid migration of lithium ions.[13] However, the reduction stability of SN is poor. Catalyzed by lithium, the −C≡N group can spontaneously polymerize to form harmful byproducts, leading to irreversible interfacial corrosion of the active lithium metal and severely reducing the cycle life.[16] In addition, the film-forming properties of SN is low and is exacerbated by the encapsulation of high concentrations of Li-salts due to plasticization. Therefore, the wide practical application of SPCE in LMB is limited.

Recently, the introduction of well-designed polymer matrices into SPCE can improve their film-forming properties. In addition, the reduction stability at the lithium−metal interface is favored by coordinating the α-hydrogen of SN with the electron-rich functional groups of polymers.[17] However, the introduction of polymers may also reduce the ionic conductivity of SPCE and alter the conduction mechanism of lithium ions.[18] Typically, SN and lithium salts form a solvated structure of [SN−Li^+] at room temperature, where the nitrogen atom in SN is the main complexation site for lithium ions.[19] With the introduction of polymers, the lithium ion transport pathway is transformed into a [polymer−Li^+] and polymer−[SN−Li^+] structure, providing a pathway for lithium ion conduction through the polymer segments.[19,20] Thus, in addition to anchoring SN, polymers may result in relatively restricted ion transport. In addition, polymer matrices have poor thermal stability and flame retardancy and may decompose or even burn under extreme conditions.[9,21] Therefore, the development of SPCE systems combining high electrochemical stability, high ionic conductivity, and excellent flame retardancy to realize high-safety, long-life semisolid LMBs remains a significant challenge.

Herein, we propose a versatile molecular engineering strategy that in situ constructs a robust cross-linked polymer framework for semisolid electrolytes, which effectively integrating the aforementioned merits (Figure 1). This approach employs a concentrated SPCE composed of a 3 M lithium bis(trifluoromethanesulfonyl)imide (LiTFSI) and SN, donated as SL, to serve as an efficient medium for ion transport

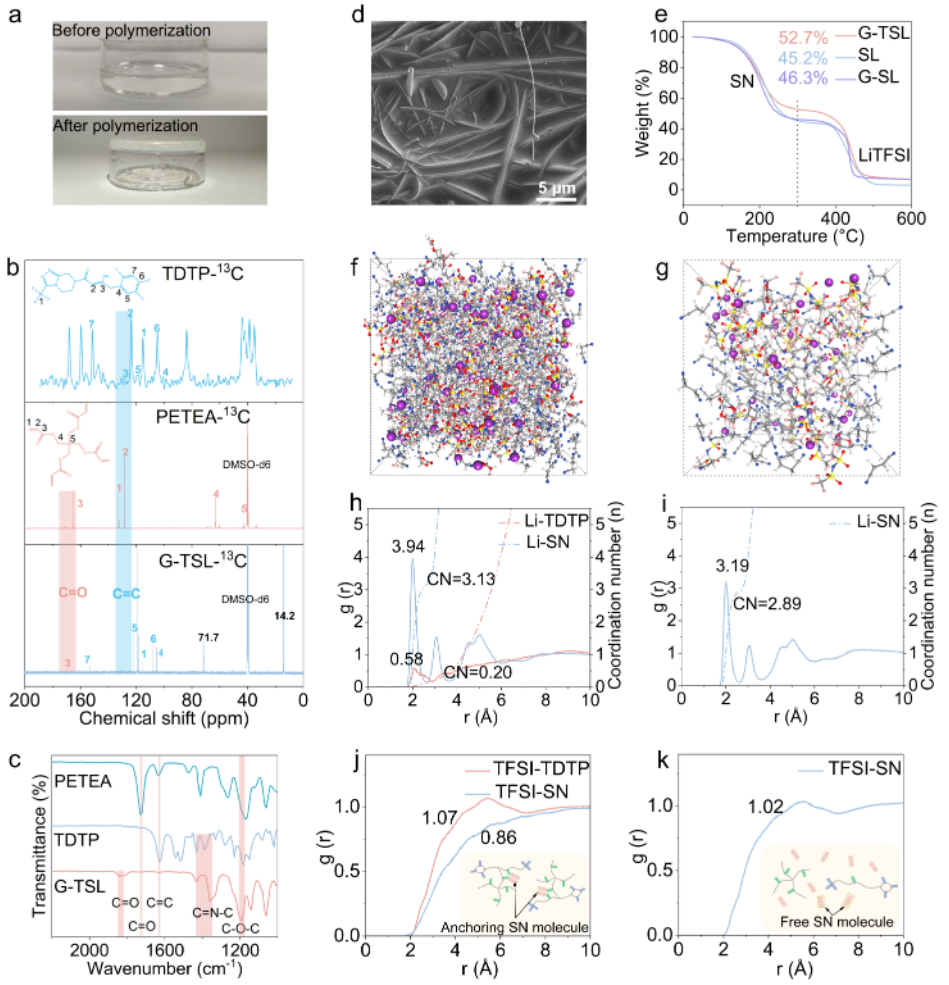

Figure 2. (a) Digital photos of precursors and G-TSL. (b) ^{13}C SSNMR spectra of TDTP and ^{13}C NMR spectra of PETEA and G-TSL. (c) FTIR spectra of PETEA, TDTP and G-TSL. (d) G-TSL polymerized on glass fiber membranes. (e) TGA of G-TSL,G-SL and SL. Snapshots of MD simulations of (f) G-TSL and (g) SL. RDF, $g(r)$ and CN of (h) G-TSL and (i) SL with Li^+. RDF, $g(r)$, and coordination number of (j) G-TSL and (k) SL with $TFSI^-$.

within semisolid electrolytes and allow it with excellent cathode stability and nonflammability. In this SPCE, a (2Z)-4-oxo-4-[3-(trifluoromethyl)-5,6-dihydro-[1,2,4]triazolo[4,3-*a*]pyrazine-7(8H)-yl]-1-(2,4,5-trifluorophenyl)-2-en-2-amine (TDTP) monomers with multiple elements (nitrogen, fluorine) and groups (benzene ring, pyrazine) was selected as the main body of the multifunctional polymer chain segment. Pentaerythritol tetraacrylate (PETEA), a cross-linking monomer with four reactive acrylate functional groups and highly polar segments, forms a robust three-dimensional cross-linked network structure via in situ polymerization with SPCE. In addition, multiple negatively charged carbonyl groups in PETEA segments and TDTP can synergistically anchor with SN by electrostatic adsorption, which significantly enhances SN's stability against lithium metal, particularly under high-temperature conditions. To further stabilize the electrode−electrolyte interface, an appropriate quantity of fluoroethylene carbonate (FEC) additive is incorporated. This design strategy allows the electrolyte to coordinate with Li ions with unique interactions, facilitating rapid Li-ion transport through weak coordination with polymer chain segments. Simultaneously, the strong interaction between the polymer matrix and SN enhances mutual solubility, reduces SN crystallinity, and facilitates the formation of rapid ion-conductive pathways (polymer−[SN−Li^+]). The resultant electrolyte can effectively stabilize the Li anode through the formation of robust LiF/Li_3N-rich SEI. Furthermore, it reduces fire risks by cothermally decomposing to release fire-extinguishing gases such as CO_2 and NH_3, while also leveraging the nonflammable properties of SN. As a proof of concept, the fabricated semisolid LMB demonstrates enhanced cycling stability at both room temperature and high temperatures (60 °C). Moreover, this molecular engineering strategy has been applied to improve the thermal stability and safety in the pouch cell, advancing the application of semisolid LMB under extreme conditions.

RESULTS/DISCUSSION

Design of Semisolid Polymer Electrolyte and the Physical Properties. The three-dimensional cross-linked semisolid polymer electrolyte (G-TSL) was synthesized via in situ polymerization of a homogeneous solution consisting of TDTP monomer and PETEA, immersed within a concentrated SPCE (3 M LiTFSI in SN with 5 wt% FEC) with thermal initiator azodiisobutyronitrile (AIBN) at 60 °C (Figure S1). The polymerization process is initiated by the thermal activation of AIBN, which decomposes into free radicals. These radicals react with the π-electron cloud of the

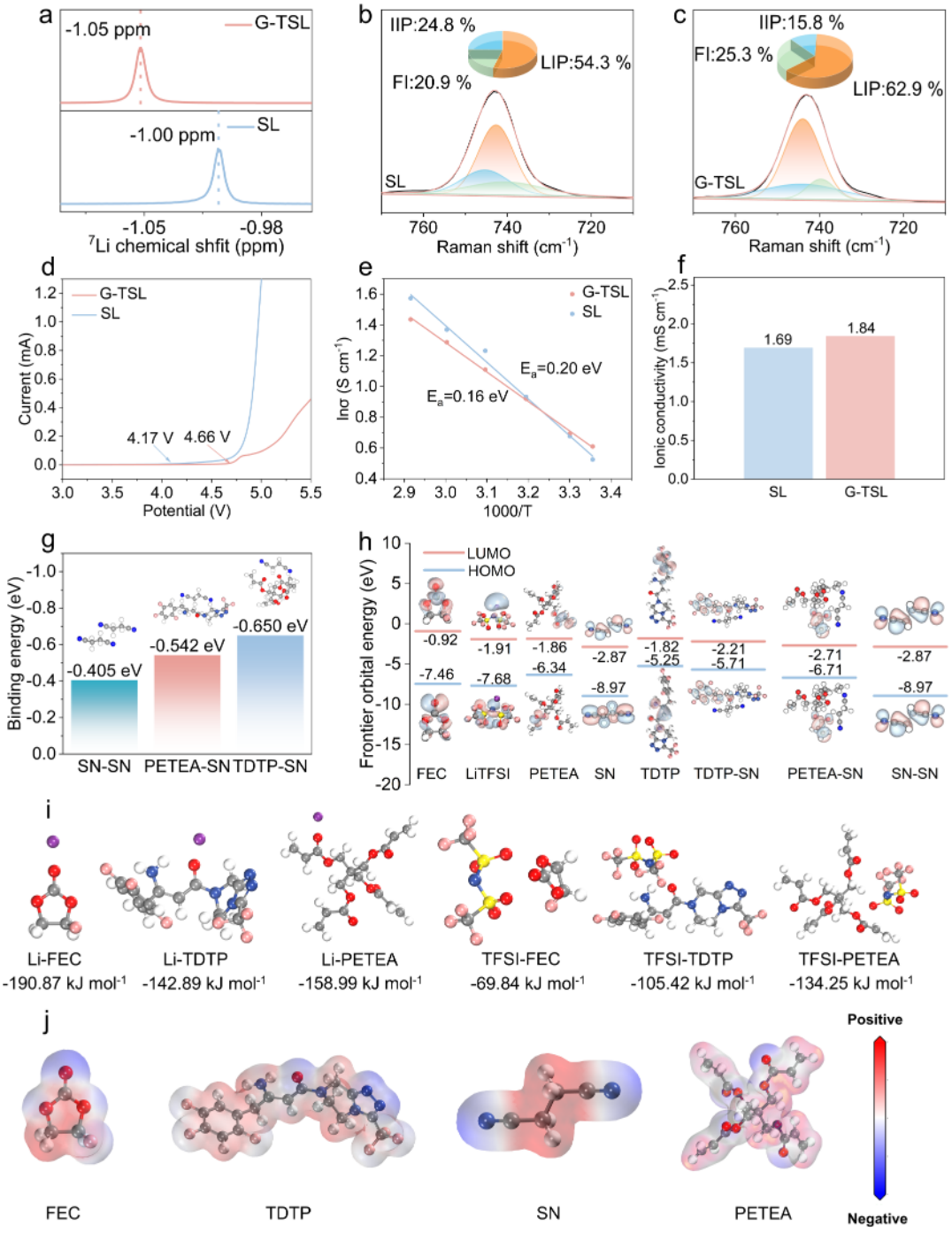

Figure 3. (a) Solid-state ^{7}Li NMR spectra in different electrolytes. Raman spectra of TFSI^{-} of (b) SL and (c) G-TSL. (d) LSV curves of different electrolytes. (e) Arrhenius plots of ionic conductivity of different electrolytes at 25−80 °C. (f) Room-temperature ionic conductivities of G-TSL and SL. (g) Binding energies of TDTP−SN, PETEA−SN, and SN−SN. (h) HOMO and LUMO energies for different components in the electrolyte. (i) Binding energies of different systems. (j) Optimized geometrical configurations and electrostatic potentials of FEC, TDTP, SN and PETEA.

monomer's double bonds (C═C), initiating radical chain formation. Subsequently, the initiating radical chains engage in continuous reactions with additional monomer molecules present in the reaction mixture, leading to chain elongation and cross-linking events that ultimately yield network structures. This transformation results in the conversion of the initially flowing, transparent precursor solution into an immobile, milky gel-like system (Figure 2a).

The polymer structure and polymerization were confirmed through solid-state nuclear magnetic resonance (SSNMR) spectroscopy, as illustrated in Figure 2b. The ^{13}C SSNMR spectrum reveals distinct peaks corresponding to the C═O at 165.4 ppm, C−F at 115.1 ppm, and characteristic peaks of the benzene ring at 105.4, 118.8, 104.7, and 151.3 ppm. These peaks originate from the C═O in PETEA, C−F bonds, and the benzene rings in TDTP, respectively. Notably, the peaks associated with the C═C groups from TDTP (123.7 ppm)

and PETEA (128.2 ppm) are completely absent after polymerization, confirming the successful cross-linking of TDTP and PETEA monomers.[22] Additional peaks at 71.7 and 14.2 ppm correspond to quaternary carbon and methylene peaks ($-CH_2-CH_2-$) generated during polymerization. To further analyze the chemical state of G-TSL, Fourier transform infrared spectroscopy (FTIR) was employed (Figure 2c). The characteristic peaks around 1730 cm^{-1}, 1630 cm^{-1}, 1430 cm^{-1}, and 1170 cm^{-1} correspond to the stretching vibrations of C═O, C═C, C═N−C, and C−O−C. The disappearance of the characteristic C═C bond peaks at 1630 cm^{-1} for both TDTP and PETEA further corroborates the successful polymerization of the matrix.[23,24] Consequently, G-TSL demonstrates a robust, dense cross-linked network that significantly increases the amorphous regions of SN. This structural configuration is expected to extend the ion transport pathways, facilitating uniform Li-ion conduction.

To investigate the microscopic structure of G-TSL, scanning electron microscopy (SEM) was employed to visualize its morphological characteristics on glass fiber substrates (Figure 2d). In contrast to the unmodified glass fiber membrane (Figure S2), SEM images reveal that the G-TSL-modified glass fiber exhibits a dense and uniform microstructure. This modification fully fills the interstitial spaces within the glass fiber matrix, forming continuous lithium-ion conductive channels that significantly facilitate Li^+ transport.[25] Thermogravimetric analysis (TGA) was conducted to evaluate the thermal stability of the polymer electrolyte (Figure 2e). To investigate whether the enhanced thermal stability of the G-TSL polymer originates from TDTP incorporation rather than PETEA, a control experiment was performed using G-SL (without TDTP). While the initial decomposition temperatures of G-TSL, G-SL, and SL showed comparability, significant differences emerged at elevated temperatures. Notably, SL demonstrated accelerated decomposition compared to the other samples as temperature increased. At 300 °C, SL and G-SL exhibit higher mass losses of 54.8% and 53.7%, respectively, contrasting with G-TSL's lower mass loss of 47.3%.[26,27] Importantly, when LiTFSI began decomposing, G-TSL displays reduced thermal weight loss relative to both SL and G-SL. These observations collectively indicate that TDTP incorporation primarily drives the thermal stability improvement in G-TSL, while PETEA contributes minimally to this enhancement.

Molecular dynamics (MD) simulations were employed to delve deeper into the coordination environment of Li^+ within different electrolyte systems. MD simulation snapshots (Figure 2f,g) reveal that the cross-linked G-TSL structure (Figure 2f) exhibits a more compact and denser morphology compared to its counterparts. To quantitatively analyze the coordination behavior of Li^+ and $TFSI^-$ within the polymer electrolyte, we performed detailed calculations of the radial distribution function (RDF), $g(r)$ and coordination number (CN) for Li−O interactions. As illustrated in Figure 2h, the RDF analysis shows that the peak for Li−TDTP at 0.58 Å is notably weaker with the smallest CN, indicating a reduced interaction between Li^+ and TDTP. This suggests that more Li^+ ions are released from strong coordination sites, enhancing their mobility. In contrast, the Li−SN coordination exhibits a pronounced peak at 3.94 Å with a CN of 3.13, highlighting a robust interaction between Li^+ and SN molecules. Within the SL system (Figure 2i), both the $g(r)$ and CN values for Li−SN interactions are relatively lower, suggesting less effective coordination. Furthermore, the RDF analysis of $TFSI^-$ interactions reveals that the dominant peak for $TFSI^-$−TDTP is significantly stronger ($g(r)$ = 1.07) compared to $TFSI^-$−SN in the SL system (Figure 2k). This indicates that TDTP not only effectively anchors the anionic $TFSI^-$ but also facilitates the binding of SN molecules within the G-TSL framework, which achieves efficient Li^+ transport through the electrolyte.

Lithium-Ion Transport Mechanism of Semisolid Polymer Electrolyte. The superior Li-ion mobility in the G-TSL electrolyte was evidenced by ^{7}Li NMR spectroscopy, as depicted in Figure 3a. The significant negative chemical shift observed for G-TSL indicates the highest extent of shielding of the lithium nucleus, suggesting that a substantial portion of Li^+ are effectively dissociated.[28] Concurrently, the ^{19}F NMR spectrum (Figure S3) shows a rightward shift for G-TSL, indicating the greatest shielding effect on the fluorine nucleus within this electrolyte. This implies that Li^+exhibit weak coordination with $TFSI^-$ in G-TSL, facilitating rapid Li^+ migration. Raman spectroscopy further validates the coordination environment of $TFSI^-$, as illustrated in Figure 3b,c. The Raman spectra distinguish between intimate ion pairs (IIP), where $TFSI^-$ interacts directly with Li^+; free $TFSI^-$ ions (FI), which do not interact with Li^+; and loose ion pairs (LIP), where $TFSI^-$ indirectly interacts with Li^+. In the G-TSL electrolyte, LIP and FI dominate, reflecting the weak interaction between Li^+ and $TFSI^-$. This observation aligns with the findings from the ^{19}F NMR spectrum,[29] reinforcing the notion of enhanced Li^+ mobility due to reduced coordination with $TFSI^-$. At a scan rate of 1 mV s^{-1}, G-TSL achieved a higher electrochemical window of 4.66 V compared to 4.17 V for SL (Figure 3d). This enhanced electrochemical stability is attributed to the presence of the cross-linked structure and nitrile groups in G-TSL, which contribute to its more stable electrochemical properties.

The G-TSL electrolyte exhibits a significantly higher Li-ion transference number (t_{Li}^+) of 0.70 compared to that of SL (0.49) (Figures S4 and S5), primarily attributed to the strong confinement of $TFSI^-$ anion transport within the polymer framework. This higher t_{Li}^+ effectively mitigates polarization effects and promotes a more uniform Li deposition behavior, enhancing battery performance. X-ray diffraction (XRD) analysis (Figure S6) reveals no characteristic peaks corresponding to crystalline phases of SN in G-TSL, suggesting that SN exhibits amorphous characteristics within this system. This amorphous nature, combined with strong interactions between SN and the polymer matrix, likely contributes to the enhanced ionic conductivity observed. Differential scanning calorimetry (DSC) measurements (Figure S7) indicate a low glass transition temperature (T_g, −33.2 °C) for the G-TSL, further supporting the hypothesis of free Li^+ migration facilitated by the amorphous regions. To investigate the Li-ion conduction behavior in G-TSL, ionic conductivities were measured over a temperature range from 25 to 70 °C were measured (Figure S8). G-TSL demonstrates excellent agreement with the linear Arrhenius equation, indicating efficient decoupling of Li^+ from the polymer backbone and coupling with SN (Figure 3e). In addition, G-TSL exhibits a notably reduced activation energy (E_a) of 0.16 eV compared to that of SN (0.20 eV), which can be attributed to the increased interaction between Li^+ and SN. At room temperature, G-TSL achieves an ionic conductivity of 1.84 mS cm^{-1}, surpassing the value of 1.69 mS cm^{-1} for SN (Figure 3f). These findings underscore that the robust

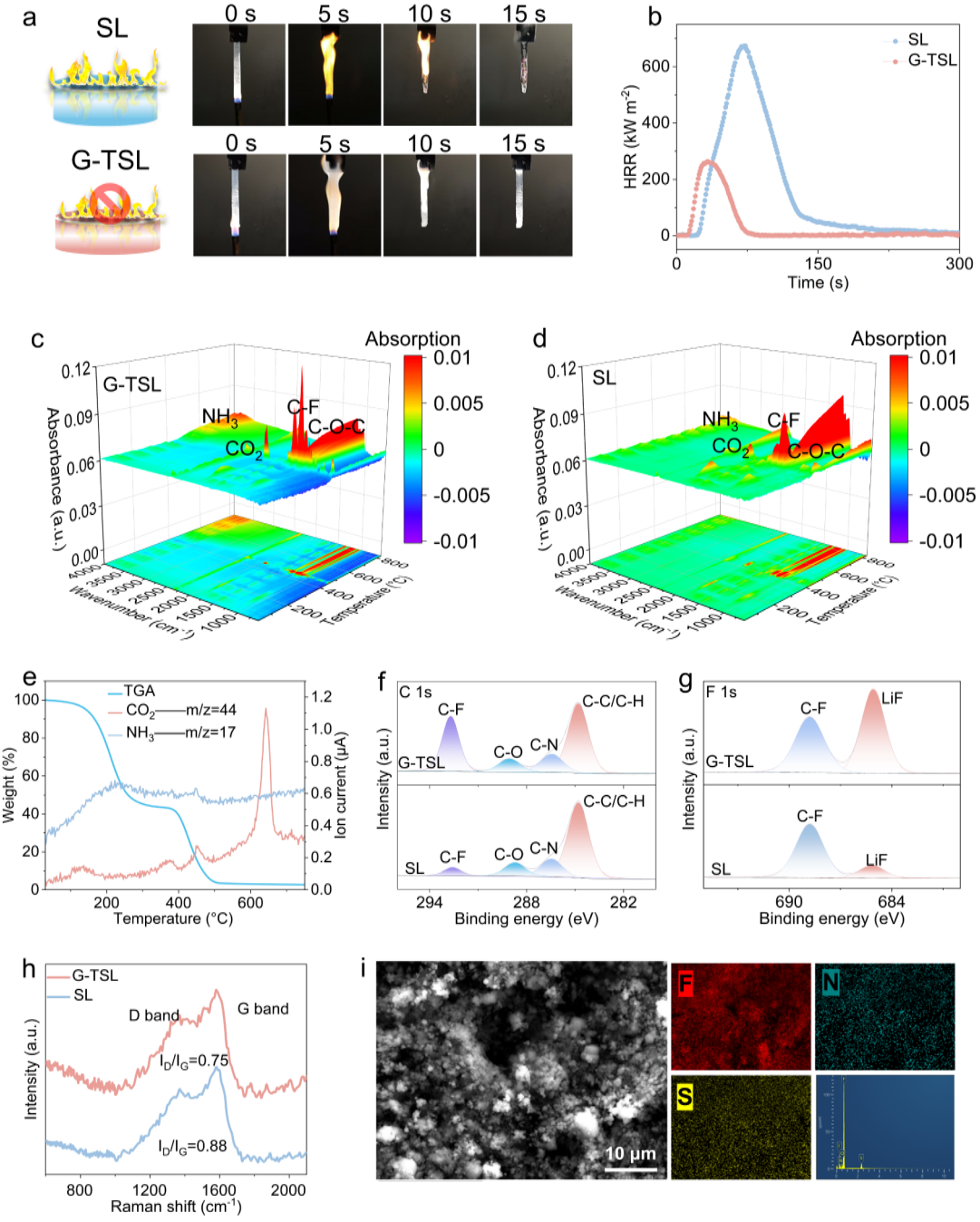

Figure 4. (a) Combustion tests of G-TSL and SL. (b) HRR curves of G-TSL and SL. TG-FTIR 3D mapping curves for (c) G-TSL and (d) SL. (e) TG-MS curve of G-TSL. XPS analysis of residual carbon in (f) G-TSL and (g) SL after combustion.(h) Raman analysis of residual carbon in two electrolytes. (i) SEM of carbon residue in G-TSL.

interaction between the cross-linked polymer network and SN increases the number of amorphous SN regions. Consequently, the weaker interactions between Li^+ and the polymer matrix enable a greater number of Li^+ to be conducted through polymer−[SN−Li^+] pathways, thus facilitating rapid Li-ion transport kinetics.

To further elucidate the coordination structure in G-TSL, density functional theory (DFT) calculations were performed to evaluate the binding energies of TDTP−SN, PETEA−SN, and SN−SN (Figure 3g). The calculations show that the binding energy of TDTP−SN (−0.65 eV) is lower than that of PETEA−SN (−0.542 eV) and SN−SN (−0.405 eV).[30] This indicates that, upon incorporation into the polymer system, SN molecules exhibit a greater affinity for the negatively charged carbonyl groups (C═O) of the polymers rather than engaging in self-association or side reactions with lithium metal in their free state. Further DFT analysis was performed to calculate and interpret the energy values of the highest occupied molecular orbital (HOMO) and the lowest unoccupied molecular orbital (LUMO) for each component of the electrolyte precursors (Figure 3h). Notably, SN, acting as the sole solvent, exhibits the lowest LUMO energy value (−2.87 eV) compared to TDTP and PETEA, signifying its reduced stability against reduction and propensity for side reactions. Upon interaction with the negatively charged C═O bonds in TDTP and PETEA, the LUMO energy values of SN increased to −2.21

eV and −2.71 eV, respectively. This charge induction strategy effectively enhances the reduction stability of SN, mitigating its tendency to undergo undesirable side reactions. Additionally, LiTFSI displays a lower LUMO energy value (−1.91 eV), indicating a higher reactivity toward reduction at the lithium anode and a significant role in SEI formation. Comparing FEC and TDTP, TDTP exhibits a lower LUMO value (−1.82 eV) compared to FEC (−0.92 eV), indicating that TDTP is more readily susceptible to electron exposure during the polymerization process.

DFT calculations were performed to investigate the adsorption energies of Li^+ and $TFSI^-$ on various polymer fragments (Figure 3i). Compared to Li^+−FEC (−190.87 kJ mol^{-1}) and Li^+−PETEA (−158.99 kJ mol^{-1}) fragments, the Li^+−TDTP fragment has a lower binding energy (−142.89 kJ mol^{-1}). This reduced binding energy can be attributed to the fluorine groups on the polymer chains reduce the nucleophilicity of oxygen atoms, resulting in weaker binding strength between O and Li^+. Consequently, this facilitates the migration of Li^+ ions with a lower barrier along the polymer chains. Additionally, the binding energy of $TFSI^-$ anions with TDTP (−105.42 kJ mol^{-1}) is notably higher than with FEC (−69.84 kJ mol^{-1}), suggesting that TDTP exhibits a stronger affinity for anchoring $TFSI^-$ anion. This enhanced anchoring capability of TDTP promotes the free movement of Li^+ ions by reducing their association with $TFSI^-$, thus improving ion mobility within the electrolyte. The interactions between polymer fragments and Li^+ are further elucidated through electrostatic potential (ESP) calculations (Figure 3j). Blue ESP surfaces denote electrophilic regions, whereas red surfaces signify nucleophilic regions. The ESP map of FEC reveals that the negative potentials are predominantly localized around O and F atoms. Additionally, significant negative charges are observed near the carbonyl groups of both TDTP and PETEA. Through electrostatic attraction between oppositely charged regions, TDTP and PETEA can effectively anchor free SN molecules. However, in the case of TDTP, the presence of fluorine atoms with substantial negative charge affects the Li−O coordination. The higher density of fluorine atoms in TDTP weakens the interaction between its oxygen atoms and Li^+, leading to increased positive charge accumulation near the oxygen atoms and a corresponding reduction in the interaction strength between Li^+ and TDTP. This observation aligns with the calculated adsorption energies.

Theoretical calculations substantiate that within the post-cross-linked polymer matrix, the robust adsorption of $TFSI^-$ by TDTP facilitates efficient Li^+ release and accelerated migration, while the anchored SN molecules via carbonyl groups mitigate lithium dendrite formation and side reactions. Furthermore, the weak coordination between TDTP and Li^+ enables a greater number of Li^+ to participate in SN solvation coupling, thereby promoting rapid Li^+ transport through continuous polymer−[SN−Li^+] conduction pathways (Figure S9). This series of theoretical calculations show that due to the weak coordination behavior of TDTP and Li^+, more Li^+ to participate in the coupling of SN, facilitating rapid transport of Li ions through the polymer−[SN−Li^+] pathways.

Fire and Thermal Safety Evaluation of Semisolid Polymer Electrolyte. Figure 4 illustrates the combustion tests of G-TSL (or SL) composites with glass fiber films, while Figure S10 provides a comparison using pure G-TSL without the glass fiber film. Impressively, the introduction of a polymer skeleton significantly enhances the flame retardancy of G-TSL. This enhanced property is attributed to the release of fire-extinguishing gases such as NH_3 and CO_2, thereby inhibiting the combustion process. To further evaluate the high-temperature dimensional stability of the G-TSL electrolyte, infrared thermography was employed. As depicted in Figure S11, thermal imaging confirmed the superior thermal stability of G-TSL compared to polypropylene (PP) diaphragm and SL electrolytes. While PP and SL electrolytes exhibited progressive shrinkage as temperatures increased, G-TSL remained dimensionally stable even at a high temperature of 180 °C, underscoring its exceptional thermal stability.[31] Cone calorimeter tests were conducted to simulate fire scenarios more rigorously.[32] As shown in Figure 4b, the heat release rate (HRR) of G-TSL is markedly lower than that of SL. Specifically, the peak HRR for G-TSL (263.4 kW m^{-2}) is considerably lower than that of SL (673.7 kW m^{-2}), indicating a slower thermal decomposition rate and reduced flame spread rate for G-TSL during a fire event, thereby mitigating fire hazards. Additionally, the total heat release (THR), detailed in Figure S12a, quantifies the cumulative heat heat generated by complete combustion. G-TSL exhibits significantly lower total heat release compared to SL, highlighting the substantial improvements in thermal stability imparted by the incorporation of TDTP. In fire conditions, the dangers posed by smoke and toxic gases often exceed those from flames and high temperatures. Therefore, the smoke production rate (SPR) and total smoke production (TSP), presented in Figure S12b,c, respectively, demonstrate that G-TSL possesses excellent smoke suppression properties, further enhancing its safety profile.

To investigate the thermal cleavage of G-TSL at elevated temperatures, in situ thermogravimetric analysis coupled with Fourier-transform infrared spectroscopy (TG-FTIR) was employed to analyze the pyrolysis products of G-TSL and SL, as illustrated in Figure 4c,d. The spectra reveal characteristic peaks corresponding to NH_3 at 3583 cm^{-1}, CO_2 at 2361 cm^{-1}, C−O−C bonds at 1200 cm^{-1}, and C−F bonds at 1088 cm^{-1}. Notably, the intensity of the peaks for C−F bonds, CO_2, and NH_3 is significantly stronger for G-TSL compared to SL. This indicates that G-TSL requires a higher heat input to break the C−F bond due to its more stable structure, which decomposes only after absorbing substantial thermal energy. Upon reaching the decomposition temperature of various functional groups, G-TSL releases a greater amount of noncombustible gases, such as CO_2, enhancing its flame-retardant properties. Moreover, the peak absorption intensity around 2926 cm^{-1}, associated with hydrocarbon compounds, is markedly lower for G-TSL, suggesting a reduced production of combustible substances during thermal degradation.[33−35] This observation underscores the significant role of TDTP in altering the pyrolysis process, leading to enhanced thermal stability and reduced flammability. To further corroborate the TG-FTIR findings, thermogravimetric analysis mass spectrometry (TG-MS) was conducted to examine the gaseous components produced during thermal decomposition (Figure 4e). As the temperature increased, the carbon chains and pyrazine bonds gradually decomposed, releasing CO_2 and NH_3. These results provide additional evidence supporting the superior flame-retardant performance of G-TSL.[36]

The composition of residual carbon is pivotal in determining the flame-retardant properties of electrolytes. To investigate this, X-ray photoelectron spectroscopy (XPS) was utilized to analyze the combustion products for residual carbon content.

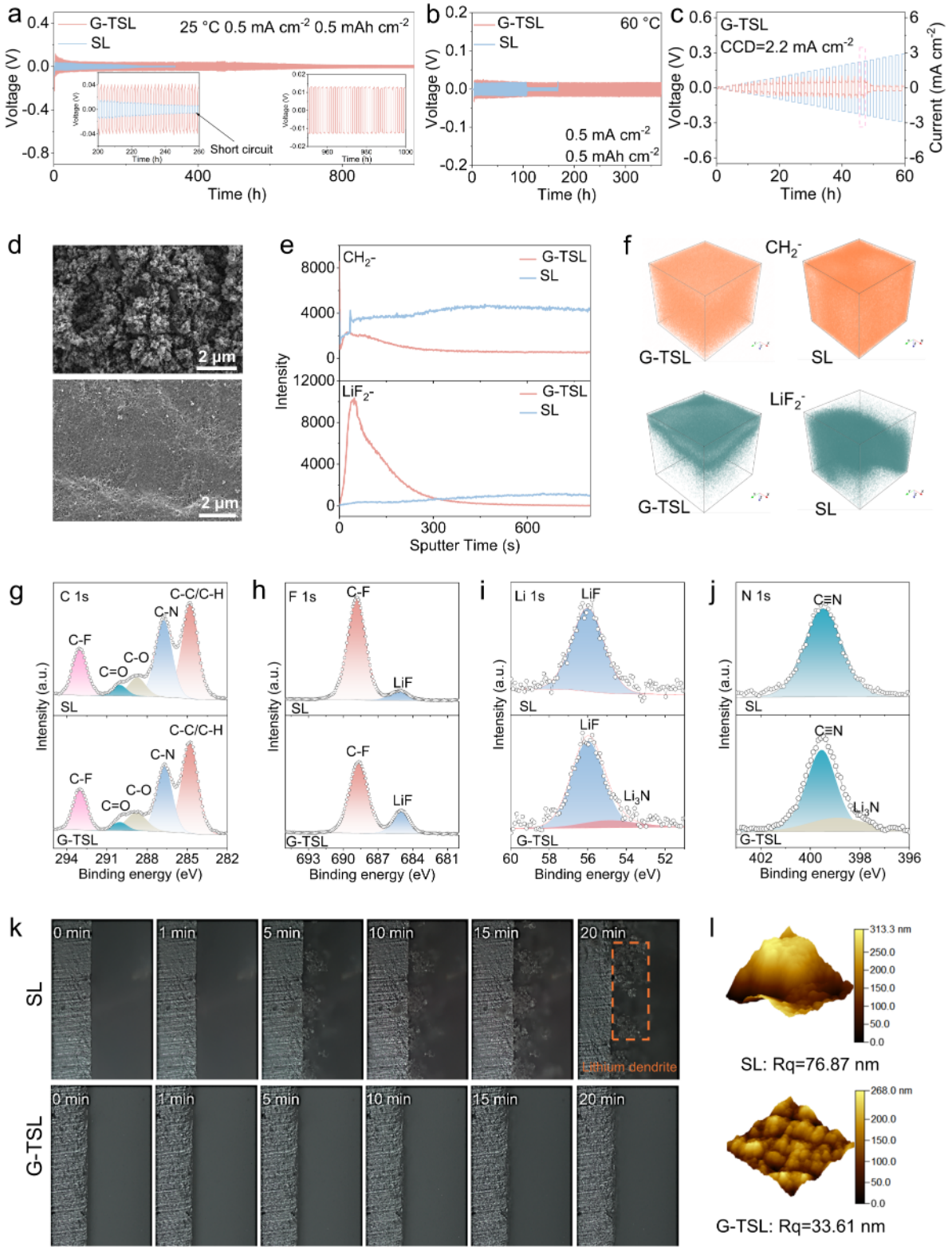

Figure 5. Cycling performance of Li symmetrical cells with two electrolytes at 0.5 mA cm^{-2} at (a) room temperature and (b) 60 °C. (c) CCD of Li symmetrical cells with G-TSL. (d) SEM image of cycled Li anodes after 100 h (25 °C, 0.5 mA cm^{-2}). (e) Intensity sputtering distribution maps corresponding to CH_2^- and LiF_2^- and (f) 3D reconstructed distribution maps. XPS of (g) C 1s, (h) F 1s, (i) Li 1s, and (j) N 1s on cycled Li anodes. (k) In-situ optical microscope image of lithium deposition behavior on the cross-section anode. (l) AFM surface and 3D morphology analysis of lithium deposition after 100 h at 0.5 mA cm^{-2}.

As illustrated in Figure 4f,g, the C 1s spectra reveal a significantly higher abundance of C−F bonds in G-TSL compared to SL, while the F 1s spectra indicate that G-TSL produces more LiF upon combustion, contributing to its superior heat and flame resistance.[37] Regarding the graphitization degree of residual carbon, it can be assessed through the

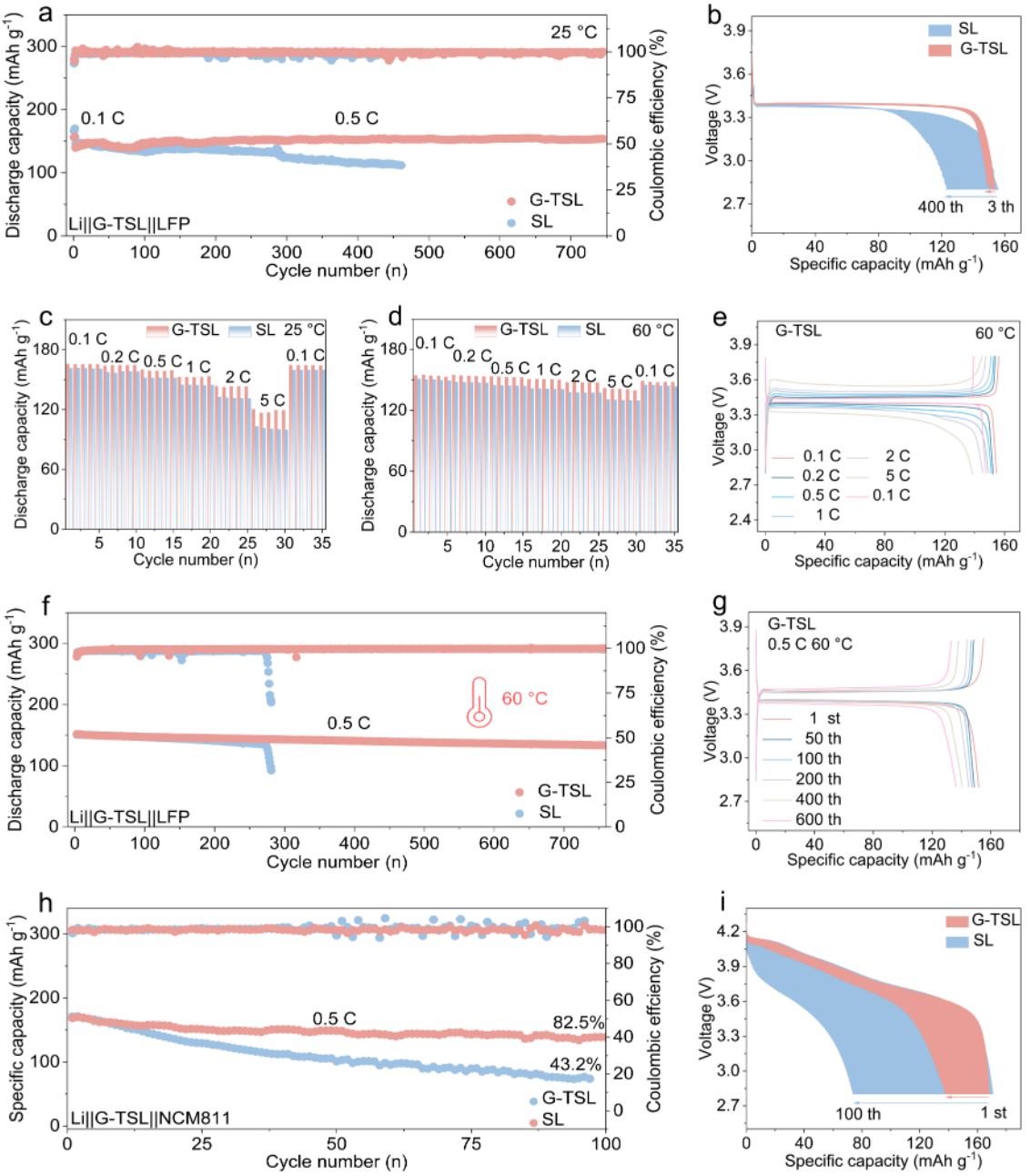

Figure 6. (a) Cycling performance of Li||G-TSL||LFP at 0.5 C and (b) corresponding charge−discharge curves. (c) Rate performance of Li|| G-TSL||LFP and Li||SL||LFP cells at 25 °C and (d) 60 °C. (e) Rate charge−discharge curves of Li||G-TSL||LFP at 60 °C. (f) Cycling performance of Li||G-TSL||LFP and Li||SL||LFP cells at 0.5 C and 60 °C. (g) Charge−discharge curve of Li||G-TSL||LFP cell at 60 °C. (h) Cycling performance of Li||G-TSL||NCM811 cell at 0.5 C at 25 °C and (i) corresponding charge−discharge curves.

intensity ratio of the D band to the G band (I_D/I_G). According to Figure 4h, G-TSL exhibits a combined (I_D/I_G) ratio of 0.75, markedly lower than the 0.88 observed for SL. This suggests that the incorporation of TDTP facilitates the formation of a more stable residual carbon layer postcombustion,[26] enhancing its structural integrity and thermal stability. To elucidate the mechanisms behind G-TSL's enhanced flame retardancy, FTIR and SEM analyses were conducted on the combustion products. The FTIR analysis (Figure S13) of G-TSL's residual carbon highlights the predominance of C−F bonds among the combustion products.[38] This indicates that during combustion, the unique monomers and cross-linkers in G-TSL generate a higher quantity of robust C−F bonds. The high bond energy of C−F absorbs substantial heat upon polymer heating, thereby reducing surface temperature and slowing combustion rates.[35] Furthermore, SEM coupled with energy-dispersive X-ray spectroscopy (EDS) provided elemental analysis of the G-TSL electrolyte's combustion products (Figure 4i). These products are composed of C, O, N, F, and S elements, with F being most abundant due to fluorinated monomers and a minor presence of FEC.[39] The molecular design of G-TSL thus further enhances the flame retardance of SN-based electrolytes, underscoring its effectiveness as a fire-safety electrolyte.

Li Metal Morphology and Interfacial Chemistry. The influence of G-TSL on the lithium metal anode was assessed through the assembly and testing of lithium symmetrical cells.

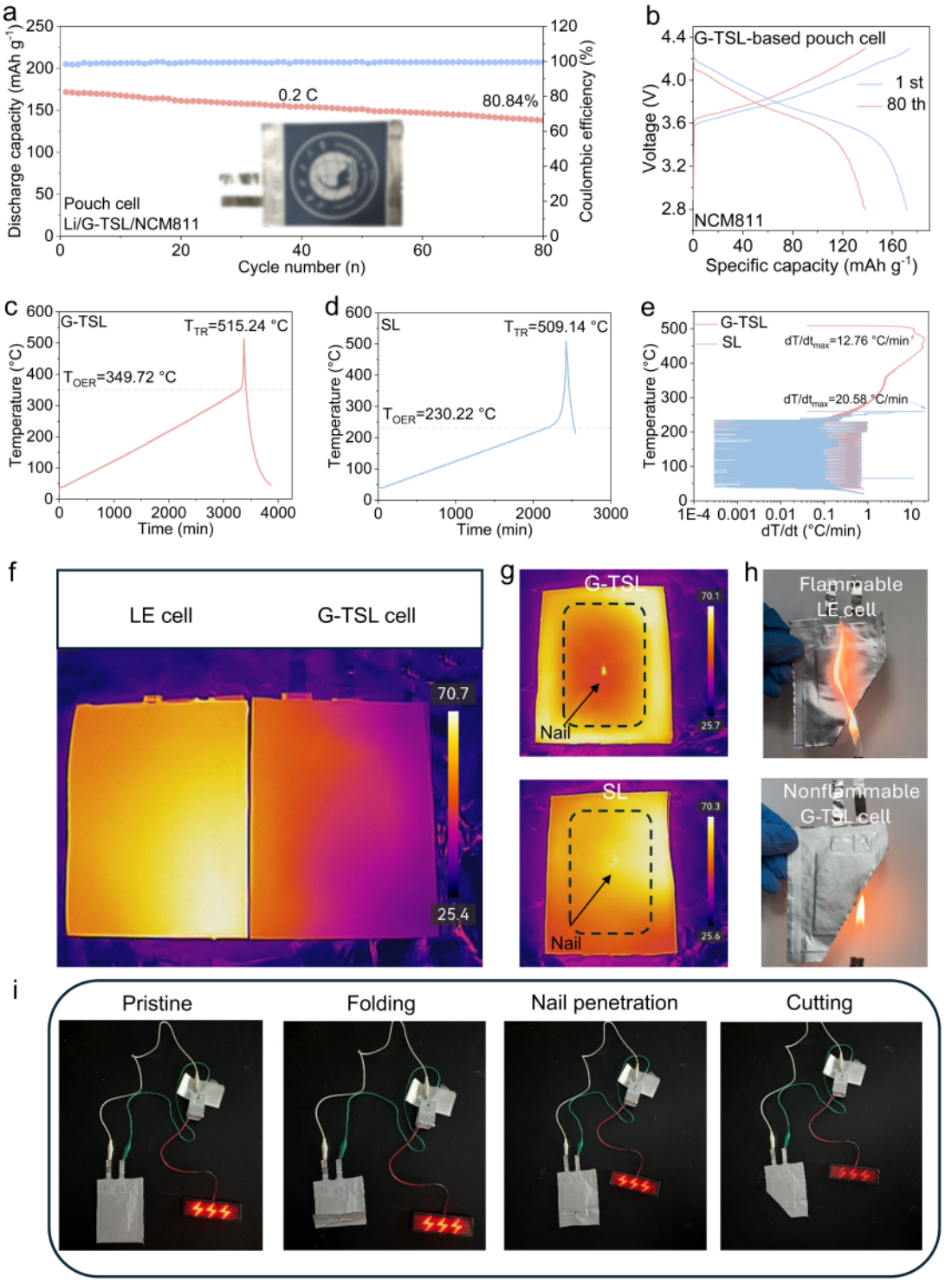

Figure 7. (a) Cycling performance of G-TSL-based pouch cell and (b) corresponding charge−discharge curve. ARC tests of fully charged (c) Li||G-TSL||NCM811 and (d) Li||SL||NCM811 pouch cells in HWS mode and (e) corresponding dT/dt vs temperature curves. Infrared thermography photos of two pouch cells under (f) overheat and (g) nail penetration conditions. (h) Ignition tests of two pouch cells. (i) Digital photographs of G-TSL-based pouch cells powering LED under various harsh conditions.

As depicted in Figure 5a, the Li||G-TSL||Li coin-type cell demonstrates exceptional stability, cycling continuously for 1000 h at room temperature, in stark contrast to the Li||SL||Li cell, which begins to short-circuit after only 250 h. Additionally, Figure 5b illustrates the Li||Li cycling performance of both cells at 60 °C. It is evident that the G-TSL electrolyte also maintains stable cycling for 360 h at elevated temperatures, highlighting its robustness under more challenging thermal conditions. To evaluate the critical current density (CCD) of both electrolytes, a rate performance test was conducted with stepwise increases in current densities from 0.1 to 5 mA cm^{-2} (Figure 5c). Notably, G-TSL exhibits a CCD exceeding 2.2 mA cm^{-2}, indicative of its superior capability to tolerate higher current densities without compromising performance. This

enhanced current tolerance is crucial for practical applications requiring high power densities. In addition, the Li||G-TSL||Cu half cell (Figure S14) maintains a higher Coulombic efficiency of 91.8% after 300 cycles. SEM images of the lithium metal surface postcycling (Figures 5d and S15) provide visual evidence of the improved deposition behavior facilitated by G-TSL. These images reveal that lithium deposition in G-TSL-based cells is notably uniform, whereas SL-based cells exhibit severe lithium dendrites and dead lithium formations. This observation suggests that G-TSL not only enhances Li-ion transport kinetics but also effectively suppresses interfacial parasitic reactions, leading to a more even and stable Li deposition.

To investigate the distribution of the SEI formed on the lithium anode after 50 cycles, time-of-flight secondary ion mass spectrometry (TOF-SIMS) was employed. The analysis revealed that in G-TSL, the content of CH_2^- organic components is notably lower compared to SL, as evidenced by the sum composition curves (Figure 5e) and three-dimensional distribution maps (Figure 5f). Importantly, the SEI in G-TSL exhibits a thin profile with a higher concentration of LiF_2^- and LiN^- species (Figure S16), indicative of a stratified structure characterized by an outer organic layer and an inner inorganic layer enriched with LiF. This layered architecture is further supported by the negative mode mapping distributions of selected charged segments (Figure S17).[40,41] XPS was utilized to delve deeper into the chemical composition of the SEI.[42] In G-TSL, there is a significant reduction in the C−F peak (Figure 5g), suggesting enhanced participation of F atoms in the formation of LiF. Additionally, the content of LiF, as observed in the F 1s spectrum (Figure 5h,i), and Li_3N, also detected in the F 1s spectrum (Figure 5i,j), significantly increases due to the presence of multifunctional polymer chain segments. LiF, known for its high surface energy,[20] and Li_3N, recognized for facilitating fast Li^+ transport,[24] contribute to the robustness of this LiF/Li_3N-rich SEI.

The dynamic lithium plating process was investigated using in situ optical microscopy (Figure 5k). During discharge at a current density of 0.5 mA cm^{-2}, the lithium electrode surface in the SL electrolyte cell exhibited noticeable dendrite formation within 5 min, with extensive dendritic lithium coverage observed after 20 min. In stark contrast, the G-TSL electrolyte maintained a smooth and compact electrode surface throughout the entire process, displaying only a small amount of uniform and dense lithium deposition even after 20 min. Atomic force microscopy (AFM) analysis (Figure 5i) further corroborates these observations, indicating that G-TSL achieves a markedly lower roughness (R_q = 33.61 nm) for the lithium deposition layer.[39] This smoother deposition profile underscores the superior ability of G-TSL to inhibit dendrite formation and promote uniform lithium plating.

Electrochemical Performance of Semisolid Lithium Metal Batteries. The electrochemical performance of the G-TSL electrolyte was further evaluated by assembling a Li||G-TSL||LFP coin-type cell, with detailed results presented in Figures 6a,b, and S18. After an initial activation at 0.1 C at room temperature, the discharge capacity of the Li||G-TSL|| LFP cell exhibits a steady increase, reaching a remarkable 153.68 mAh g^{-1} after 745 cycles. In stark contrast, the capacity of the Li||SL||LFP cell diminishes to 115.8 mAh g^{-1} after only 400 cycles. The discharge curves depicted in Figure 6b clearly illustrate this disparity: while the capacity of the Li||G-TSL|| LFP cell remains relatively stable over 400 cycles, the Li||SL|| LFP cell experiences a significant decline in capacity. To assess the rate performance, tests were conducted at various current densities (Figure 6c). The Li||G-TSL||LFP cell demonstrated reversible capacities of 165.6 mAh g^{-1} (0.1 C), 164.6 mAh g^{-1} (0.2 C), 159.9 mAh g^{-1} (0.5 C), 153.3 mAh g^{-1} (1 C), 143.4 mAh g^{-1} (2 C), and 120.1 mAh g^{-1} (5 C). These values significantly outperform those of the Li||SL||LFP cell, which recorded capacities of 161.4, 156.5, 151.8, 144.6, 132.5, and 99.6 mAh g^{-1}, respectively. The enhanced rate performance of the Li||G-TSL||LFP cell underscores the faster Li-ion migration facilitated by the G-TSL electrolyte.

To further explore the advantages of G-TSL under high-temperature conditions, the cycling performance of the Li||G-TSL||LFP coin-type cell was evaluated at an extreme temperature of 60 °C. Figure 6d,e, along with Figure S19, illustrate the rate performance and charge−discharge curves at 0.5 C and 60 °C, demonstrating that the Li||G-TSL||LFP cell retains a capacity of 141.8 mAh g^{-1} even at the high current density of 5 C. Figure 6f,g, alongside Figure S20, present the cycling performance and charge−discharge curves of both Li|| G-TSL||LFP and Li||SL||LFP cells at 60 °C. After 750 cycles, the Li||G-TSL||LFP cell maintains a capacity of 133.5 mAh g^{-1}, corresponding to an impressive capacity retention rate of 87%. In stark contrast, the capacity of the Li||SL||LFP cell drops precipitously after just 250 cycles. Moreover, the potential of G-TSL in Li||NCM811 cell was further evaluated. As shown in Figure 5h,i, the Li||G-TSL||NCM811 cell achieves a capacity retention rate of 82.5% after 100 cycles at 0.5 C, while the control group exhibits a mere 43.2% retention rate over the same period. These results highlight the versatility and robustness of G-TSL, demonstrating its suitability not only for stable operation at elevated temperatures but also for high-voltage applications.

Safety Evaluation of Semisolid Lithium Metal Pouch Cell. To evaluate the safety and reliability of G-TSL in practical applications, the G-TSL was further assessed in a Li|| NCM811 pouch cell. Prior to this evaluation, the cycle stability of the pouch cell was validated, achieving 80 cycles with a capacity retention of 80.84%, at 0.2C (Figure 7a,b). To precisely analyze the thermal safety, the heat generated by the fully charged cells in an adiabatic environment was measured using accelerating rate calorimetry (ARC) with the typical heat-wait-search (HWS) mode.[33] For comparative analysis, we also evaluated a commercial carbonate liquid electrolyte (LE) consisting of 1 M $LiPF_6$ in EC/DEC (vol % 1:1). The exothermic reaction onset temperature (T_{OER}) and thermal runaway temperature (T_{TR}) were defined based on warming rates of 0.02 °C min^{-1} and 10 °C min^{-1}, respectively. As illustrated in Figure 7c,d, the T_{OER} for G-TSL is significantly higher at 349.72 °C compared to SL (230.22 °C) and LE (122.9 °C). Additionally, the T_{TR} for pouch cells with G-TSL (515.24 °C) and SL (509.14 °C) is notably elevated compared to LE (356.03 °C). These findings indicate that G-TSL effectively inhibits exothermic reactions at high temperatures and significantly delays thermal destruction. More importantly, the highest temperature rising rate (dT/dt) for the G-TSL-based cell is only 2% of that observed in the LE-based cell, as shown in Figures 7e, S21, and Table S1. These results underscore the superior thermal stability and safety profile of G-TSL, making it a highly promising candidate for enhancing the safety and reliability of lithium metal batteries in practical applications.

As illustrated in Figure 7f, infrared thermography reveals the distribution of internal temperatures during heating, demonstrating that the G-TSL-based pouch cell maintains a lower temperature compared to the LE counterpart, even under high-temperature conditions. This trend is further corroborated by puncture tests (Figure 7g), where the internal temperature of the G-TSL-based cell remains significantly lower, indicating minimal heat release and enhanced safety. To assess the performance under extreme conditions, an open-flame ignition experiment was conducted on the cell components (Figure 7h). The results show that the G-TSL pouch cell does not ignite or burn when exposed to flames, whereas the leaked LE exhibits violent combustion upon flame exposure. Furthermore, the fully charged G-TSL-based pouch cell demonstrates remarkable stability and safety under various mechanical stress tests. It continues to power an LED without experiencing internal short circuits or combustion, even after undergoing artificial bending, nail penetration, and cutting (Figures 7i). These findings highlight the robust safety profile of G-TSL in semisolid LMB, making it highly suitable for real-world applications where safety and reliability are paramount.

CONCLUSIONS

In summary, this work demonstrates a versatile molecular engineering strategy for in situ constructing semisolid electrolytes with high ionic conductivity, electrochemical stability, and flame retardancy, which is suitable for lithium metal batteries with high safety and long cycling life. The strong anchoring effect between the cross-linked network polymer and SN as well as the weak coordination between the Li-ion and the polymer promote the establishment of the fast ion conductive path (polymer−[SN−Li^+]). At the same time, this constructed semisolid electrolyte forms a LiF/Li_3N-rich SEI during the cycling, which effectively stabilizes the lithium anode interface and achieves uniform lithium deposition behavior. In addition, the nonleakage of the cross-linked network and the intrinsic nonflammability of the plastic crystal electrolyte further enhance the safety of the semisolid electrolyte. These properties allow semisolid lithium metal batteries to exhibit enhanced cyclic stability at both room temperature and high temperatures (60 °C). Furthermore, this strategy has been successfully verified in the Li||$LiNi_{0.8}Co_{0.1}Mn_{0.1}O_2$ pouch cell under extreme conditions, which provides a promising solution for the practical application of semisolid lithium metal batteries.

EXPERIMENTAL METHODS

Electrolyte Preparation. All chemicals were used as received without further purification. The concentrated (3 mol L^{-1}) SN-LiTFSI electrolyte (SL) was prepared by dissolving 0.852 g of LiTFSI (99%, Aladdin), 0.95 g of SN (99%, Aladdin) and 0.05 g of FEC (98%, Aladdin). For the synthesis of concentrated SPCE, TDTP (98%, Aladdin) and PETEA (80%, Aladdin) with a molar ratio of 1:1 were added into the SL (the mass fraction of TDTP/PETEA to SL was 1.95%) followed by stirring for 2 h. After that, 0.1 wt % of AIBN (98%, Aladdin) was introduced as a thermal initiator and stirred for another 30 min to obtain the G-TSL electrolyte precursor. The cell assembly was conducted in an argon-filled glovebox, after which polymerization was carried out at 70 °C for 2 h in a temperature-controlled oven. Both electrolyte preparation and cell assembly processes were strictly performed under inert conditions within the glovebox. For comparison, a conventional electrolyte (1 M $LiPF_6$ in EC/DEC, 1:1 v/v) was also employed. Notably, all cells were assembled using conventional fabrication procedures, with the sole distinction being the substitution of liquid electrolyte with a polymerizable precursor solution. Following encapsulation, the cells underwent thermal treatment at 70 °C for 2 h in a controlled oven environment to facilitate complete polymerization.

Cathode Preparation. Commercial LFP and NCM811 powders were employed as cathode active materials. The cathodes were fabricated by thoroughly mixing 80 wt % active material, 10 wt% conductive carbon (Super P), and 10 wt % polyvinylidene difluoride (PVDF) binder in 1-methyl-2-pyrrolidinone (NMP) to form a homogeneous slurry. The slurry was then uniformly coated onto an aluminum foil current collector using a doctor blade, followed by vacuum drying at 80 °C for 12 h to ensure complete solvent removal.

Characterization. FTIR was conducted on a Thermo Fisher Scientific Nicolet iS20 spectrometer. Solid-state NMR spectra were acquired using a Bruker Avance Neo 400WB. Solution-state NMR ($^1H/^7Li$) spectra were recorded on a Bruker Ascend 600 MHz spectrometer (DMSO-d_6). Pyrolysis products were analyzed using a thermogravimetric mass spectrometry analyzer (TGA, Netzsch STA 449 F3). The glass transition temperatures (T_g) were determined by DSC (TA Q2000, DSC2500). XRD patterns were collected on a Rigaku MiniFlex 600 diffractometer. Raman spectra were recorded on a Renishaw inVia spectrometer. Cone calorimetry tests (Suzhou VOUCH 6810) employed a 25 KW m^{-2} heat flux. XPS data were acquired on a Thermo Scientific K-Alpha spectrometer. TOF-SIMS was conducted using an IONTOF instrument. Horizontal-vertical flammability tests followed the FTT0082 standard. In situ Li deposition was monitored via optical microscopy (ZOOM-0850C, Puqian Optical) at 0.5 mA cm^{-2} (Li working electrode). Cyclic deposition morphologies were characterized using AFM. TG-MS analysis was performed under argon at 10 °C min^{-1} to 800 °C. TG-IR was performed under nitrogen (50 mL min^{-1}, 10 °C min^{-1} to 800 °C) with spectral detection at 500−4000 cm^{-1}.

Cell Assembly and Measurements. EIS measurements (0.1−10^6 Hz, 25−70 °C) were performed on a BioLogic SP-150 electrochemical workstation to determine ionic conductivity (σ) using the following equation:

$$\sigma = \frac{L}{R_b} \tag{1}$$

where L and S are the thickness and area of G-TSL, respectively, and R_b is the bulk impedance.

The LSV was conducted using Li|stainless steel cells at a scan rate of 1 mV s^{-1} from 0 to 6 V. The activation energy was derived from Arrhenius equation:

$$\frac{1}{R_0} = A\exp\left(-\frac{E_a}{RT}\right) \tag{2}$$

where R_0 represents the Li^+ desolvation or interphase transport resistance, T is the absolute temperature, R is the gas constant, and A is the pre-exponential factor.

The t_{Li}^+ was determined by chronoamperometry (ΔV = 10 mV) in Li||Li symmetric cells, calculated using the following equation:

$$t_{Li}^+ = \frac{I_s(\Delta V - R_0 I_0)}{I_0(\Delta V - R_s I_s)} \tag{3}$$

where I_0 and R_0 are initial current and resistance. I_s and R_s are steady-state values.

CR2032 coin cells were assembled to evaluate electrochemical performance, consisting of prepared LFP (or NCM811) cathodes and Li metal anodes with different electrolytes. Celgard 2500 was used as the separator. After a 6-h resting period, cells underwent initial activation at 0.1 C before cycling testing.

Computational Methods. All calculations were performed using Materials Studio with the DMol3 code. The Perdew−Burke−Ernzerhof (PBE) functional within the generalized gradient approximation (GGA) was utilized to compute the exchange-correlation energy. During geometry optimization, the double numerical plus polarization (DNP) basis set and all-electron core

treatment were selected. The van der Waals interactions were described using the DFT-D method of Grimme. The convergence tolerances of energy change, maximum force, and maximum displacement were set as 1×10^{-5} Ha, 0.002 Ha/Å, and 0.005 Å, respectively.

MD simulations were performed using the Forcite modules. Molecules including FEC, PETEA, TDTP, SN, AIBN, and LiTFSI were got geometry optimization through Dmol3 software. The A electrolyte system was built by Amorphous Cell module: 500 SN, 100 LiTFSI, 24 FEC, 6 AIBN, 20 PETEA-TDTP. The B electrolyte system was built by Amorphous Cell module:500 SN, 100 LiTFSI, 24 FEC. COMPASSII force field was adopted for all molecules. The systems were pre-equilibrated using the NPT ensemble at 298 K for a duration of 50 ps, followed by equilibration under the NVT ensemble at 298 K for 1 ns to achieve the final stable state. The final 500 ps of the NVT production steps were utilized to sample data for radial distribution function (RDF) and coordination structure counting analyses.

AUTHOR INFORMATION

Corresponding Authors

Anjun Hu − *College of Materials and Chemistry & Chemical Engineering (College of Lithium Resources and Lithium Battery Industry), Chengdu University of Technology, Chengdu 610059, China;* orcid.org/0000-0003-4025-0330; Email: anjunhu@cdut.edu.cn

Jianping Long − *College of Materials and Chemistry & Chemical Engineering (College of Lithium Resources and Lithium Battery Industry), Chengdu University of Technology, Chengdu 610059, China;* orcid.org/0000-0001-7245-8991; Email: longjianping@cdut.cn

Gang Wu − *The Collaborative Innovation Center for Eco-Friendly and Fire-Safety Polymeric Materials (MoE), National Engineering Laboratory of Eco-Friendly Polymeric Materials (Sichuan), State Key Laboratory of Polymer Materials Engineering, College of Chemistry, Sichuan University, Chengdu, Sichuan 610064, China;* Email: gangwu@scu.edu.cn

Authors

Kai Chen − *College of Materials and Chemistry & Chemical Engineering (College of Lithium Resources and Lithium Battery Industry), Chengdu University of Technology, Chengdu 610059, China*

Guo-Rui Zhu − *The Collaborative Innovation Center for Eco-Friendly and Fire-Safety Polymeric Materials (MoE), National Engineering Laboratory of Eco-Friendly Polymeric Materials (Sichuan), State Key Laboratory of Polymer Materials Engineering, College of Chemistry, Sichuan University, Chengdu, Sichuan 610064, China*

Yuanjian Li − *Institute of Materials Research and Engineering (IMRE), Agency for Science, Technology and Research (A*STAR), Singapore 138634, Singapore*

Jingyun Jiang − *Institute of Materials Research and Engineering (IMRE), Agency for Science, Technology and Research (A*STAR), Singapore 138634, Singapore*

Borui Yang − *College of Materials and Chemistry & Chemical Engineering (College of Lithium Resources and Lithium Battery Industry), Chengdu University of Technology, Chengdu 610059, China*

Ting Li − *College of Materials and Chemistry & Chemical Engineering (College of Lithium Resources and Lithium Battery Industry), Chengdu University of Technology, Chengdu 610059, China*

Kun Li − *College of Materials and Chemistry & Chemical Engineering (College of Lithium Resources and Lithium Battery Industry), Chengdu University of Technology, Chengdu 610059, China*

Jingze Chen − *College of Materials and Chemistry & Chemical Engineering (College of Lithium Resources and Lithium Battery Industry), Chengdu University of Technology, Chengdu 610059, China*

Wang Xu − *College of Materials and Chemistry & Chemical Engineering (College of Lithium Resources and Lithium Battery Industry), Chengdu University of Technology, Chengdu 610059, China*

Zhen Wang − *College of Materials and Chemistry & Chemical Engineering (College of Lithium Resources and Lithium Battery Industry), Chengdu University of Technology, Chengdu 610059, China*

Ruize Xu − *College of Materials and Chemistry & Chemical Engineering (College of Lithium Resources and Lithium Battery Industry), Chengdu University of Technology, Chengdu 610059, China*

Wei Yang − *College of Materials and Chemistry & Chemical Engineering (College of Lithium Resources and Lithium Battery Industry), Chengdu University of Technology, Chengdu 610059, China*

Jian Wang − *Helmholtz Institute Ulm (HIU), Ulm D89081, Germany; Karlsruhe Institute of Technology (KIT), Karlsruhe D-76021, Germany;* orcid.org/0000-0002-7945-0826

Zhi Wei Seh − *Institute of Materials Research and Engineering (IMRE), Agency for Science, Technology and Research (A*STAR), Singapore 138634, Singapore;* orcid.org/0000-0003-0953-567X

Author Contributions

K.C.: Conceptualization, Visualization, Methodology, Writing − original draft. A.H.: Investigation, Writing − review and editing. G.-R.Z.: Conceptualization, Visualization. Y.L.: Conceptualization, Visualization. J.J.: Investigation, Writing − review and editing. B.Y.: Formal analysis. T.L.: Validation. K.L.: Validation. J.C.: Conceptualization, Visualization. W.X.: Formal analysis, Validation. Z.W.: Formal analysis, Validation. R.X.: Formal analysis. W.Y.: Formal analysis. J.W.: Validation. G.W.: Writing − review and editing, Validation. J.L.: Writing − review and editing, Funding acquisition, Project administration, Supervision. Z.W.S.: Funding acquisition, Supervision, Validation.

Notes

The authors declare no competing financial interest.

ACKNOWLEDGMENTS

This work was supported by the Key Laboratory of Sichuan Province for Lithium Resources Comprehensive Utilization and New Lithium Based Materials for Advanced Battery Technology (LRMKF202405), the National Natural Science Foundation of China (52402226), the Natural Science Foundation of Sichuan Province (2024NSFSC1016), and the Scientific Research Startup Foundation of Chengdu University of Technology (10912-KYQD2023-10240), the Singapore National Research Foundation (NRF Investigatorship NRF-NRFI09-0002), and the Agency for Science, Technology and Research (MTC Programmatic Fund M23L9b0052). We would like to thank shiyanjialab (www.shiyanjia.com) for their support with XPS tests and SCI-GO (www.sci-go.com) for their assistance with Raman tests, and we appreciate Phadcalc (www.phadcalc.com) for providing the molecular dynamics simulation services.

REFERENCES

(1) Zhang, W.; Koverga, V.; Liu, S.; Zhou, J.; Wang, J.; Bai, P.; Tan, S.; Dandu, N. K.; Wang, Z.; Chen, F.; Xia, J.; Wan, H.; Zhang, X.; Yang, H.; Lucht, B. L.; Li, A.-M.; Yang, X.-Q.; Hu, E.; Raghavan, S. R.; Ngo, A. T.; Wang, C. Single-Phase Local-High-Concentration Solid Polymer Electrolytes for Lithium-Metal Batteries. *Nat. Energy* **2024**, *9* (4), 386−400.

(2) Tan, J.; Ma, L.; Yi, P.; Wang, Y.; Li, Z.; Fang, Z.; Li, X.; He, S.; Wang, X.; Ye, M.; Shen, J. Scalable Customization of Crystallographic Plane Controllable Lithium Metal Anodes for Ultralong-Lasting Lithium Metal Batteries. *Adv. Mater.* **2024**, *36* (30), 2403570.

(3) Wang, L.; Zhou, Z.; Yan, X.; Hou, F.; Wen, L.; Luo, W.; Liang, J.; Dou, S. X. Engineering of Lithium-Metal Anodes Towards a Safe and Stable Battery. *Energy Storage Mater.* **2018**, *14*, 22−48.

(4) Tan, S.-J.; Wang, W.-P.; Tian, Y.-F.; Xin, S.; Guo, Y.-G. Advanced Electrolytes Enabling Safe and Stable Rechargeable Li-Metal Batteries: Progress and Prospects. *Adv. Funct. Mater.* **2021**, *31* (45), 2105253.

(5) Yang, S.-J.; Hu, J.-K.; Jiang, F.-N.; Yuan, H.; Park, H. S.; Huang, J.-Q. Safer Solid-State Lithium Metal Batteries: Mechanisms and Strategies. *InfoMat* **2024**, *6* (2), No. e12512.

(6) Liu, X.; Jia, H.; Li, H. Flame-Retarding Quasi-Solid Polymer Electrolytes for High-Safety Lithium Metal Batteries. *Energy Storage Mater.* **2024**, *67*, 103263.

(7) Yang, B.; Hu, A.; Li, T.; Li, K.; Li, Y.; Jiang, J.; Xiao, Z.; Seh, Z. W.; Long, J. Eliminating Water Hazards and Regulating Electrode-Electrolyte Interfaces by Multifunctional Sacrificial Electrolyte Additives for Long-Life Lithium Metal Batteries. *Energy Storage Mater.* **2024**, *70*, 103512.

(8) Huo, S.; Sheng, L.; Xue, W.; Wang, L.; Xu, H.; Zhang, H.; He, X. Challenges of Polymer Electrolyte with Wide Electrochemical Window for High Energy Solid-State Lithium Batteries. *InfoMat* **2023**, *5* (3), No. e12394.

(9) Hu, A.; Chen, W.; Li, F.; He, M.; Chen, D.; Li, Y.; Zhu, J.; Yan, Y.; Long, J.; Hu, Y. Nonflammable Polyfluorides-Anchored Quasi-Solid Electrolytes for Ultra-Safe Anode-Free Lithium Pouch Cells without Thermal Runaway. *Adv. Mater.* **2023**, *35* (51), 2304762.

(10) Hao, Q.; Ma, X.; Gao, Y.; Chen, F.; Chen, X.; Qi, Y.; Li, N. Commercial Carbonate-Based Gel Polymer Electrolytes Enable Safe and Stable High-Voltage Li-Metal Batteries. *Energy Storage Mater.* **2024**, *70*, 103509.

(11) Li, T.; Chen, K.; Yang, B.; Li, K.; Li, B.; He, M.; Yang, L.; Hu, A.; Long, J. In Situ Polymerization of 1,3-Dioxolane and Formation of Fluorine/Boron-Rich Interfaces Enabled by Film-Forming Additives for Long-Life Lithium Metal Batteries. *Chem. Sci.* **2024**, *15* (30), 12108−12117.

(12) Chen, G.; Zhang, Y.; Zhang, C.; Ye, W.; Wang, J.; Xue, Z. Abundant Hydrogen Bonds Formed in a Urea-Based Gel Polymer Electrolyte Improve Interfacial Stability in Lithium Metal Batteries. *ChemSuschem* **2022**, *15*, No. e202201361.

(13) Ye, W.; Wang, J.; Shi, Z.; Guo, K.; Xue, Z. Facile Fabrication of Cross-Linked Polymer Electrolyte via Imidazole-Based Deep Eutectic Solvent-Induced in Situ Polymerizations. *J. Membr. Sci.* **2024**, *696*, 122541.

(14) Wang, J.; Zhang, C.; Zhang, Y.; Chen, G.; Poli, R.; Xie, X.; Xue, Z. Facile Assembly of C−N Bond-Containing Polymer Electrolytes Enabled by Lithium Salt-Catalyzed Aza-Michael Addition. *Macromolecules* **2023**, *56* (6), 2484.

(15) Peng, H.; Long, T.; Peng, J.; Chen, H.; Ji, L.; Sun, H.; Huang, L.; Sun, S. Molecular Design for In-Situ Polymerized Solid Polymer Electrolytes Enabling Stable Cycling of Lithium Metal Batteries. *Adv. Energy Mater.* **2024**, *14*, 2400428.

(16) Jiang, M.; Li, T.; Qiu, Y.; Hou, X.; Lin, H.; Zheng, Q.; Li, X. Electrolyte Design with Dual − C≡N Groups Containing Additives to Enable High-Voltage $Na_3V_2(PO_4)_2F_3$-Based Sodium-Ion Batteries. *J. Am. Chem. Soc.* **2024**, *146* (18), 12519−12529.

(17) Park, J.; Seong, H.; Yuk, C.; Lee, D.; Byun, Y.; Lee, E.; Lee, W.; Kim, B. J. Design of Fluorinated Elastomeric Electrolyte for Solid-State Lithium Metal Batteries Operating at Low Temperature and High Voltage. *Adv. Mater.* **2024**, *36* (30), 2403191.

(18) Xu, H.; Yang, J.; Niu, Y.; Hou, X.; Sun, Z.; Jiang, C.; Xiao, Y.; He, C.; Yang, S.; Li, B.; Chen, W. Deciphering and Integrating Functionalized Side Chains for High Ion Conductive Elastic Ternary Copolymer Solid-State Electrolytes for Safe Lithium Metal Batteries. *Angew. Chem., Int. Ed.* **2024**, *63* (36), No. e202406637.

(19) Wang, S.; Sun, Q.; Zhang, Q.; Li, C.; Xu, C.; Ma, Y.; Shi, X.; Zhang, H.; Song, D.; Zhang, L. Li-Ion Transfer Mechanism of Ambient-Temperature Solid Polymer Electrolyte toward Lithium Metal Battery. *Adv. Energy Mater.* **2023**, *13* (16), 2204036.

(20) Li, Z.; Fu, J.; Zhou, X.; Gui, S.; Wei, L.; Yang, H.; Li, H.; Guo, X. Ionic Conduction in Polymer-Based Solid Electrolytes. *Adv. Sci.* **2023**, *10* (10), 2201718.

(21) Han, L.; Wang, L.; Chen, Z.; Kan, Y.; Hu, Y.; Zhang, H.; He, X. Incombustible Polymer Electrolyte Boosting Safety of Solid-State Lithium Batteries: A Review. *Adv. Funct. Mater.* **2023**, *33* (32), 2300892.

(22) Sun, Q.; Wang, S.; Ma, Y.; Zhou, Y.; Song, D.; Zhang, H.; Shi, X.; Li, C.; Zhang, L. Fumaronitrile-Fixed In-Situ Gel Polymer Electrolyte Balancing High Safety and Superior Electrochemical Performance for Li Metal Batteries. *Energy Storage Mater.* **2022**, *44*, 537−546.

(23) Sun, Q.; Wang, S.; Ma, Y.; Song, D.; Zhang, H.; Shi, X.; Zhang, N.; Zhang, L. Li-Ion Transfer Mechanism of Gel Polymer Electrolyte with Sole Fluoroethylene Carbonate Solvent. *Adv. Mater.* **2023**, *35* (28), 2300998.

(24) Zhao, C.; Yan, Z.; Zhou, B.; Pan, Y.; Hu, A.; He, M.; Liu, J.; Long, J. Identifying the Role of Lewis-Base Sites for the Chemistry in Lithium-Oxygen Batteries. *Angew. Chem., Int. Ed.* **2023**, *62* (32), No. e202302746.

(25) Chang, H.; Li, W.; Liu, H.; Hu, H.; Liu, W.; Jin, Y.; Cui, G. Molecular Engineering of Poly (Ionic Liquid)-Based Random Copolymer Electrolytes for Enhanced Performance of Solid-State Lithium Batteries. *Chem. Eng. J.* **2024**, *481*, 148602.

(26) Yang, B.; Pan, Y.; Li, T.; Hu, A.; Li, K.; Li, B.; Yang, L.; Long, J. High-Safety Lithium Metal Pouch Cells for Extreme Abuse Conditions by Implementing Flame-Retardant Perfluorinated Gel Polymer Electrolytes. *Energy Storage Mater.* **2024**, *65*, 103124.

(27) Ling, C.; Naren, T.; Liu, X.; Yang, J.; Xiao, P.; Wei, W.; Ji, X.; Kuang, G.-C.; Chen, L. In-Situ Polymerization Induced Phase Separation to Develop High-Performance Self-Healable Polymeric Electrolytes for Lithium Metal Battery. *Mater. Today Energy* **2023**, *36*, 101372.

(28) Zhang, D.; Liu, Y.; Sun, Z.; Liu, Z.; Xu, X.; Xi, L.; Ji, S.; Zhu, M.; Liu, J. Eutectic-Based Polymer Electrolyte with the Enhanced

Lithium Salt Dissociation for High-Performance Lithium Metal Batteries. *Angew. Chem., Int. Ed.* **2023**, *62* (44), No. e202310006.
(29) Liu, Y.; Jin, Z.; Liu, Z.; Xu, H.; Sun, F.; Zhang, X.-Q.; Chen, T.; Wang, C. Regulating the Solvation Structure in Polymer Electrolytes for High-Voltage Lithium Metal Batteries. *Angew. Chem., Int. Ed.* **2024**, *63* (34), No. e202405802.
(30) Lin, C.; Yang, T.; Zhang, H.; Wang, D.; Zhang, W.; Wang, Y.; Xia, Y.; Huang, H.; Xia, X.; Gan, Y.; He, X.; Tao, X.; Zhang, J. Ternary Stabilization Strategies for Succinonitrile-Based In Situ Polymerized Electrolyte Enabling High-Performance Solid Lithium Metal Batteries. *Chem. Eng. J.* **2024**, *495*, 153541.
(31) Shi, X.; Sun, Q.; Boateng, B.; Niu, Y.; Han, Y.; Lv, W.; He, W. A Quasi-Solid Composite Separator with High Ductility for Safe and High-Performance Lithium-Ion Batteries. *J. Power Sources* **2019**, *414*, 225−232.
(32) Han, L.; Liao, C.; Liu, Y.; Yu, H.; Zhang, S.; Zhu, Y.; Li, Z.; Li, X.; Kan, Y.; Hu, Y. Non-Flammable Sandwich-Structured TPU Gel Polymer Electrolyte without Flame Retardant Addition for High Performance Lithium-Ion Batteries. *Energy Storage Mater.* **2022**, *52*, 562−572.
(33) Zhu, G.-R.; Zhang, Q.; Liu, Q.-S.; Bai, Q.-Y.; Quan, Y.-Z.; Gao, Y.; Wu, G.; Wang, Y.-Z. Non-Flammable Solvent-Free Liquid Polymer Electrolyte for Lithium Metal Batteries. *Nat. Commun.* **2023**, *14* (1), 4617.
(34) Li, P.; Wang, B.; Liu, Y.-Y.; Xu, Y.-J.; Jiang, Z.-M.; Dong, C.-H.; Zhang, L.; Liu, Y.; Zhu, P. Fully Bio-Based Coating from Chitosan and Phytate for Fire-Safety and Antibacterial Cotton Fabrics. *Carbohydr. Polym.* **2020**, *237*, 116173.
(35) Zhu, T.; Liu, G.; Chen, D.; Chen, J.; Qi, P.; Sun, J.; Gu, X.; Zhang, S. Constructing Flame-Retardant Gel Polymer Electrolytes via Multiscale Free Radical Annihilating Agents for Ni-Rich Lithium Batteries. *Energy Storage Mater.* **2022**, *50*, 495−504.
(36) Zelenková, G.; Slovák, V. Decomposition of Ammonium Salts by Quantitative TG-MS. *J. Therm. Anal. Calorim.* **2022**, *147* (24), 15059−15068.
(37) Chen, D.; Liu, Y.; Xia, C.; Han, Y.; Sun, Q.; Wang, X.; Chen, W.; Jian, X.; Lv, W.; Ma, J.; He, W. Polybenzimidazole Functionalized Electrolyte with Li-Wetting and Self-Fluorination Functionalities for Practical Li Metal Batteries. *InfoMater* **2022**, *4*, No. e12247.
(38) He, Z.; Chen, Y.; Huang, F.; Jie, Y.; Li, X.; Cao, R.; Jiao, S. Fluorinated Solvents for Lithium Metal Batteries. *Acta Phys.-Chim. Sin.* **2022**, *38* (11), 2205005.
(39) Wang, Y.; Tu, H.; Sun, A.; Wang, L.; Zhu, F.; Xue, P.; Wang, J.; Ye, F.; Liu, M. Dual Li^+ Transport Enabled by BN-assisted Solid-Polymer-Electrolyte for High-Performance Lithium Batteries. *Chem. Eng. J.* **2023**, *475*, 146414.
(40) Wu, J.; Gao, Z.; Tian, Y.; Zhao, Y.; Lin, Y.; Wang, K.; Guo, H.; Pan, Y.; Wang, X.; Kang, F.; Tavajohi, N.; Fan, X.; Li, B. Unique Tridentate Coordination Tailored Solvation Sheath Toward Highly Stable Lithium Metal Batteries. *Adv. Mater.* **2023**, *35*, No. e2303347.
(41) Mushtaq, F.; Tu, H.; Zhao, L.; Wang, L.; Tang, B.; He, Z.; Cao, Y.; Hou, Z.; Ran, J.; Wang, J.; Zahid, M.; Zhang, Y.; Liu, M. Dielectric Additive Induced Weak Li Solvation towards Stabilized Solid Electrolyte Interface for 4.6V Lithium Metal Batteries. *Energy Storage Mater.* **2024**, *73*, 103854.
(42) Wang, C.; Sun, Z.; Liu, Y.; Liu, L.; Yin, X.; Hou, Q.; Fan, J.; Yan, J.; Yuan, R.; Zheng, M.; Dong, Q. A Weakly Coordinating-Intervention Strategy for Modulating Na^+ Solvation Sheathes and Constructing Robust Interphase in Sodiummetal Batteries. *Nat. Commun.* **2024**, *15* (1), 6292.